ACS OMEGA

http://pubs.acs.org/journal/acsodf

Article

Synthesis, Characterization, and Photocatalytic, Bactericidal, and Molecular Docking Analysis of Cu−Fe/TiO_2 Photocatalysts: Influence of Metallic Impurities and Calcination Temperature on Charge Recombination

Muhammad Saqib Khan, Marcos Fernández García,* Mehraj Javed, Anna Kubacka, Uriel Caudillo-Flores, Sobia Ahsan Halim, Ajmal Khan,* Ahmed Al-Harrasi,* and Nadia Riaz*

Cite This: *ACS Omega* 2021, 6, 26108−26118

Read Online

ACCESS | Metrics & More | Article Recommendations | Supporting Information

ABSTRACT: This research evaluated the potential photocatalytic efficiency of synthesized Cu−Fe/TiO_2 photocatalysts against organic contaminants and biocontaminants through various synthesis methods (Cu-to-Fe ratio, metal loading, and calcination temperature) and reaction parameters (photocatalyst dose, irradiation time, and different initial methyl orange (MO) concentrations). In addition, the best photocatalysts were characterized through Brunauer−Emmett−Teller (BET), X-ray diffraction (XRD), differential reflectance spectroscopy (DRS), and X-ray photoelectron spectroscopy (XPS) analysis techniques. The best metal loading was 1 wt % with 5:5 Cu/Fe ratio and 300 °C calcination temperature (5Cu−5Fe/TiO_2-300) having 97% MO decolorization. Further analysis indicates that the metal presence does not generate new channels for de-excitation but clearly affects the intensity and decreases charge recombination. The behavior of the photoluminescence intensity is (inversely) proportional to the activity behavior through the series, indicating that the main catalytic effect of Fe and Cu relates to charge recombination and that the Cu−Fe bimetallic catalyst optimizes such function. Moreover, the best-engineered photocatalysts asserted impactful bacteriostatic efficacy toward the tested *Escherichia coli* strain (in 30 min), and therefore, molecular docking studies were used to predict the inhibition pathway against *E. coli* β-lactamase enzyme. The photocatalyst had a high negative docking score (−5.9 kcal mol^{-1}) due to intense interactions within the active site of the enzyme. The molecular docking study revealed that the ligand could inhibit β-lactamase from producing its bactericidal activity.

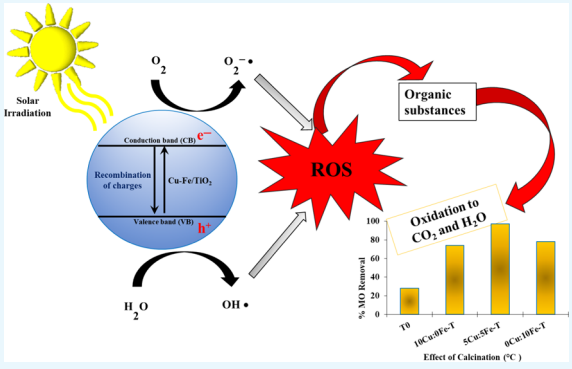

1. INTRODUCTION

Environmental pollution is the principal issue chemical scientists will face in the coming centuries on a universal scale.[1] Natural water pollution is one of the main problems of the world, which releases harmful organic and biological pollutants into the environment.[2,3] Untreated waste produced from the textile industry, hospitals, and other healthcare facilities are among the leading contributors to aquatic contamination. Such untreated wastes are characterized by toxic organic dyes and high pathogenic load responsible for the contamination of the food chain, disturbance of ecological balance, and spread of deadly infectious diseases, thus posing a threat to human health.[4] Treated or untreated hospital waste effluents are responsible for carrying and spreading pathogenic multi-drug-resistant microorganisms like *Escherichia coli* responsible for the spread of serious health infections.[5]

Among different treatment technologies to degrade a variety of organic air and water pollutants, heterogeneous photocatalysis using the semiconductor TiO_2 is extensively used.[6] Titanium dioxide, among different photocatalysts, is preferred over other materials due to its chemical stability and nontoxic nature.[7] The only limiting factor of TiO_2 in photocatalytic technology is its activation only under the UV light and its wide band gap, thus requiring energy equal to or larger than its band gap energy (E_g).[8] Other limiting factors restricting its photoactivity are ineffective visible light consumption and unrestrained electron/hole pairs recombination with a fast backward reaction.[9]

To address the aforementioned limitations, many strategies have been used, including doping semiconductors with metal or nonmetal ions, dye sensitization, and coupling with other

Received: June 13, 2021
Accepted: August 11, 2021
Published: September 28, 2021

Table 1. Application of Cu, Fe, and Cu−Fe/TiO_2 Photocatalyst for Photocatalytic Degradation of Organic Compounds in Industrial Wastewaters

photocatalysts	preparation methods	light source	applications
Fe/TiO_2	HT[a]		XRG dye[19]
Fe/TiO_2	SG[a]		MB photocatalytic degradation[20]
Fe/TiO_2	SG		photocatalytic degradation of 1,2-dichloroethane[21]
Fe/TiO_2	SG	UV	95% *E. coli* removal efficiency (0.5 mol % Fe) after 120 min[22]
Fe/TiO_2	SG	UV	*E. coli* and *Staphylococcus aureus* inactivation[23]
Cu/TiO_2	SG	UV	*E. coli*[24]
Cu/TiO_2	DP	visible	orange II photocatalytic degradation[25]
Cu−Ni/TiO_2	WI	visible	DIPA photocatalytic degradation[26]
Cu−Fe/TiO_2	SG-HT	visible	desulfurization of diesel fuel[27,28]
Cu−Ni/TiO_2	WI, DP, and CP[a]	visible	orange II photocatalytic degradation[29−31]
Cu−Ni/SiO_2	WI		hydrogen production[32]
Cu−Ni/TiO_2	SG-HT	visible	hydrogen production[33]
Cu−Ni/TiO_2	solvent hot		aminopyrine photodegradation[9]
Fe/Al_2O_3−MCM-41	SG-WI	visible	hydrogen production[34]

[a]HT, hydrothermal; SG, sol−gel; WI, wet impregnation; DP, deposition precipitation; CP, coprecipitation.

Table 2. Optimization of Synthesis Parameters, Metal Ratios, Metal Loading, and Calcination Temperature of Cu-Fe/TiO_2 Photocatalysts for Percent Decolorization of MO

	metal loading (wt %)							
	0.50	1.00	5.00	10.00	0.50	1.00	5.00	10.00
photocatalysts	300 °C				500 °C			
10Cu−0Fe/TiO_2	65.00	74.14	68.90	65.60	36.43	22.05	20.10	24.40
9Cu−1Fe/TiO_2	59.00	72.06	64.00	69.40	47.86	55.39	53.00	51.80
7Cu−3Fe/TiO_2	81.00	94.97	68.00	68.90	63.29	72.06	69.10	71.80
5Cu−5Fe/TiO_2	79.00	97.06	88.72	78.31	66.16	84.56	72.06	50.00
3Cu−7Fe/TiO_2	52.23	65.81	63.80	62.70	39.09	38.72	41.90	37.50
1Cu−9Fe/TiO_2	65.80	78.31	72.90	73.30	52.59	55.39	53.80	52.20
0Cu−10Fe/TiO_2	68.00	78.31	71.60	56.90	51.62	55.39	60.20	51.00

semiconductors by adding electron donors (hole scavengers) or carbonate salts.[10] Metal doping has been proved as the active technique to improve photocatalytic activity.[11] However, since so many features affected the photoactivity of the TiO_2 photocatalyst, the effects of metal doping, both negative and positive, have been taken into account, including the synthesis method of metal doping, metal content, type of metal, and the experimental conditions (pH and temperature).[12] Metal cations act as a trap for the electron and/or hole on the surface of TiO_2, which inhibits the electron−hole recombination, thus improving the photocatalytic activity.[13] Another outcome from metal incorporation is shifting the absorption region from the UV to the visible range by reducing the band gap between the conduction band (CB) and the valence band (VB).[14,15] Representative examples of the studies using Cu- or Fe-doped TiO_2 photocatalysts are listed in Table 1.

Moreover, recent improvements in TiO_2 photocatalysis have resulted in a series of new visible light-active photocatalysts with better characteristics, as well as a variety of fascinating surface phenomena and reaction products. The art of quantitatively modeling molecular structures and simulating their behavior using quantum mechanical methods is known as molecular modeling. For TiO_2 photocatalysis, molecular modeling approaches are critical. They employ quantum mechanical approaches, which allow us to analyze chemical events using computer computations rather than experiments.[16−18] Quantum mechanical calculations appear to be a promising method for modeling the processes and product distributions of photocatalytic degradation reactions of organic contaminants in gas and aqueous phases. Because quantum mechanical approaches are based on particle physics concepts, they could be applied to the development of novel photocatalysts.

The present study aimed to synthesize the visible light-active photocatalysts with high photocatalytic and bactericidal activity. Moreover, methyl orange (MO) of the azo class was selected as the model dye due to its frequent use in the textile industry and hospitals for the determination of organic acids in urine[35] and has been reported resistant to photodegradation and oxidation.

2. RESULTS AND DISCUSSION

2.1. Optimization of Cu and Fe Mass Composition. Results of Cu and Fe mass composition on the decolorization of MO are depicted in Table 2. Compared to the combination of Cu and Fe in the bimetallic state, monometallic 10Cu−0Fe/TiO_2 and 0Cu−10Fe/TiO_2 photocatalysts performed significantly lower for the decolorization of the MO dye. These findings are comparable to the recent reports on the use of Cu−Fe bimetallic photocatalysts in the reduction of various environmental pollutants like orange II dye, diisopropanolamine (DIPA) (alkanolamine), diclofenac, and aliphatic halogenated contaminants.[25,29,31,36−38]

2.2. Impact of the Calcination Temperature. Calcination is an important factor in controlling photocatalytic performance.[39] Influence of the calcination temperature on the performance of various synthesized photocatalysts is depicted in Table 2. The optimum calcination temperature

https://doi.org/10.1021/acsomega.1c03102
ACS Omega 2021, 6, 26108−26118

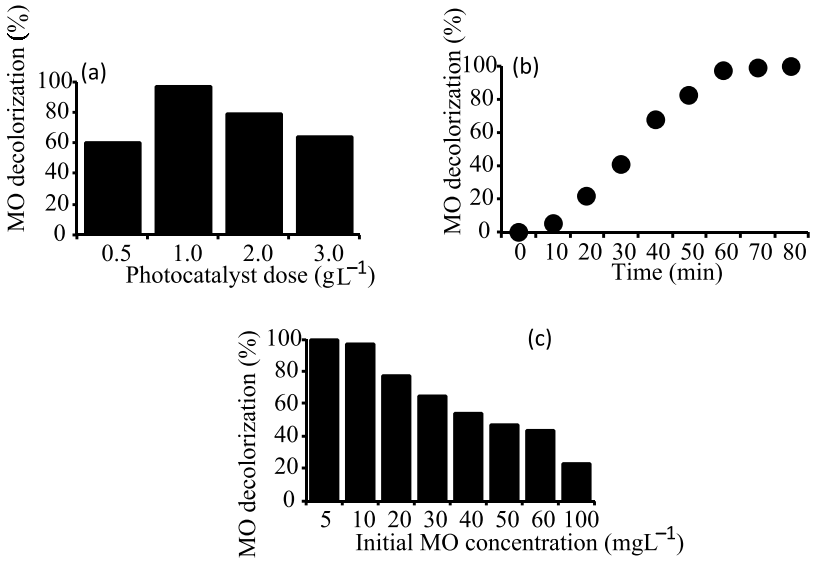

Figure 1. Effect of 5Cu−5Fe/TiO_2-300 on the decolorization efficiency of the MO dye (a) dose, (b) irradiation time, and (c) initial MO concentration.

was 300 °C with maximum MO decolorization (97.06%), while the maximum performance of the photocatalysts calcined at 500 °C was 84.56%. Similar findings were reported in a previous study[40] for the degradation of orange II dye using bimetallic photocatalysts.

2.3. Impact of the Metal Loading/Composition. The impact of different metal loadings (0.5, 1, 5, and 10 wt %) and metal compositions of Cu/Fe (0, 1, 3, 5, 7, 9, and 10) is discussed in this section. The results are depicted in Table 2 in terms of MO percentage removal. Metal loading of 1 wt % and 5:5 Cu/Fe composition showed 97.06% MO decolorization; however, the 0.5, 5, and 10 wt % showed 79, 88, and 62% decolorization of MO. Previous studies showed that higher impurity contents tend to block the active sites and hence reduce the photocatalytic performance.[41−43]

Based on the above synthesis optimization studies, 5Cu−5Fe/TiO_2-300 with 1 wt % metal loading was selected for further studies.

2.4. Effect of the Photocatalyst Dose. The effect of 5Cu−5Fe/TiO_2-300 dose (0.5, 1, 2, and 3 g L^{-1}) on the decolorization of the MO dye was evaluated, as depicted in Figure 1a. The maximum MO decolorization from 60 to 97% was observed with increasing photocatalyst dose from 0.5 to 1 g L^{-1}, respectively, while a further increase from 2 to 3 g L^{-1} resulted in a lower MO decolorization of 79 and 64%, respectively. Higher decolorization with increasing photocatalyst dose is directly linked to the availability of more active sites on the surface of the photocatalyst, which accelerates the efficiency of the photocatalyst.[44] Moreover, lower decolorization is attributed to light dispersion by an excessive dose of the photocatalysts.[45]

2.5. Effect of the Irradiation Time. The effect of the irradiation time on the decolorization efficiency of 5Cu−5Fe/TiO_2-300 for the decolorization of MO is depicted in Figure 1b. It is apparent that with an increase in irradiation time, the MO decolorization increases. In this study, 97% decolorization was achieved in 60 min of irradiation. The results of this study are well comparable to those previously obtained under UV irradiation (50% MO decolorization in 90 min of irradiation).[46]

2.6. Effect of the Initial MO Concentration. The effect of the initial concentration of MO was assessed at different initial MO concentrations (10, 20, 30, 40, 50, 60 mg L^{-1}) and keeping the other parameters constant, including photocatalyst dose (1 mg mL^{-1}), working pH, and ambient temperature 23 ± 2 °C and reaction time (60 min) (Figure 1c). The MO decolorization decreased with subsequent increment in initial MO concentration. The reason explained in the previous studies is the photon interruption at higher initial MO concentrations; moreover, at higher MO concentrations, dye molecules absorb a large amount of visible light that decreases photocatalyst effectiveness, leading to the inhibition of percent decolorization.[41−43]

2.7. Photocatalytic Kinetics for the Decolorization of MO. The pseudo-first-order (PFO) and second-order (SO) kinetics models were used for the quantitative evaluation, as depicted in Figure S1 (Supporting Information). The kinetic data best fitted into the PFO kinetic model, and K_{app} was calculated from the slope of linear regression. Similar findings were reported in previous studies on bimetallic photocatalysts, indicating that PFO is suitable for the entire range of the investigated pollutants.[26,31,37,42,47,48]

The heterogeneous photocatalytic mechanism used here is the Langmuir−Hinshelwood isotherm model (L−H), and it is the most widely used one.[41,42,49] The plot of $1/K_{app}$ against $[MO]_0$ is depicted in the inset of Figure 2, while k_c and K_{ads} obtained from the slope and intercept are 0.5296 mg L^{-1} h^{-1} and 1.2552 L mg^{-1}, respectively. The higher K_{ads} values signify a stronger adsorption, which is the most important factor in determining the photocatalytic performance of the photocatalysts.[50] Figure 2 shows the impact of the initial MO concentration on its initial photodegradation rate, which describes the fact that initial photodegradation rates escalated with increasing MO concentration and eventually became steady. Similar results are reported in previous investigations, where a strong linear fit (R^2 = 0.983) was achieved employing a Langmuir−Hinshelwood model but with a reduced rate constant (K_c = 0.792 mg L^{-1}), evidencing poor adsorption of MO on the particle surface. Broadly speaking, overall results for decaying of k_1 at increasing MO concentrations can be

https://doi.org/10.1021/acsomega.1c03102
ACS Omega 2021, 6, 26108−26118

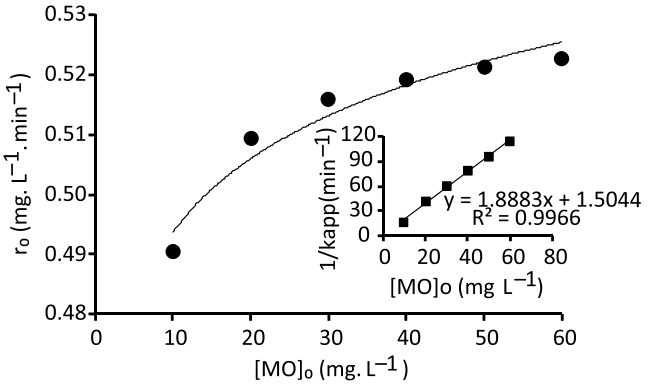

Figure 2. Effect of the MO concentration on the initial decolorization rate using 1 wt % 5Cu−5Fe/TiO_2-300; inset: plot of reciprocal of apparent rate (K_{app}).

generalized by identifying multiple aspects: (1) elevated quantities of MO molecules are adsorbed by photocatalysts on active sites, and (2) larger numbers of photons are absorbed by MO. For the latter reason, nanoparticles have fewer photons accessible, reducing the number of electron−hole pairs and thereby lowering the operational productivity of nanoparticles.[49,51]

2.8. Methyl Orange Mineralization. The amount of organic pollutant mineralization is measured by the reduction in chemical oxygen demand (COD) and total organic carbon (TO-carbon). For this purpose, COD and TO-carbon tests were performed to determine the mineralization of the MO azo dye using TiO_2-300 and 5Cu−5Fe/TiO_2-300 photocatalysts. The results are reported in % COD and TO-carbon removal, as depicted in Figure 3. The bimetallic 5Cu−5Fe/

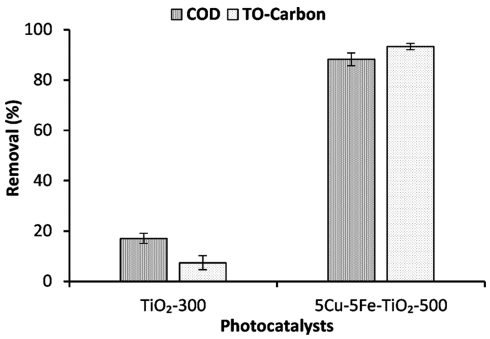

Figure 3. Effect of the synthesized photocatalyst on COD and TO-carbon (% removal) after 60 min of irradiation.

TiO_2-300 showed better COD and TO-carbon reduction of 88.21 and 93.27%, respectively, compared to the COD and TO-carbon reduction of TiO_2-300 of 17.03 and 7.4%, respectively. These results are comparable to previous studies, where 53% COD removal was obtained in 120 min of irradiation for Cu/TiO_2/ZnO photocatalysts.[52]

2.9. Photocatalytic Bactericidal Performance Evaluation and Molecular Docking Studies. Antibacterial studies were conducted using control (without the addition of a photocatalyst, only light), TiO_2-300, 5Cu−5Fe/TiO_2-300, and 5Cu−5Fe/TiO_2-500 photocatalysts against the human pathogen, *E. coli*. The results depicted in Figure 4a,b show a complete reduction (%) and inactivation (CFU mL^{-1}) of *E. coli* in 30 min of irradiation, whereas upon increasing the

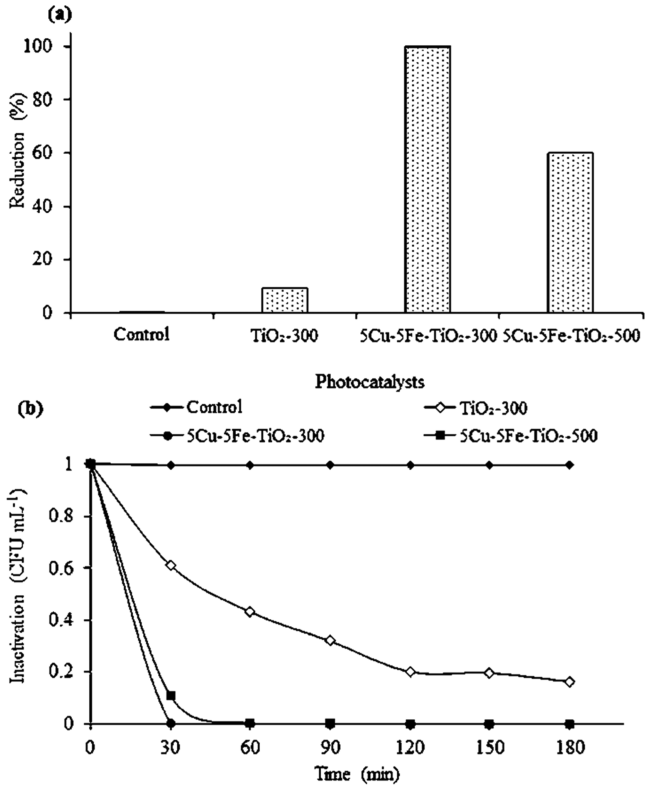

Figure 4. Bactericidal performance of the synthesized photocatalysts: (a) reduction (%) in 30 min of irradiation and (b) inactivation (kill time required for complete inactivation).

calcination temperature, the photocatalytic activity decreased to 60%. The present study observed excellent photobiocidal efficiency with a 100% drop (in 30 min) in the growth of bacteria when metallic ions were doped with TiO_2. However, TiO_2-300 (as a positive control) showed a reduction in bacterial growth of just 9% under visible light irradiation. The main catalytic effect of the Fe and Cu relates to charge recombination, and the Cu−Fe bimetallic catalyst optimizes such function as indicated by the X-ray photoelectron spectroscopy (XPS) study. In parallel, bioactivity can result from photocatalyst cessations or direct association with *E. coli*.[53] The binding of the photocatalyst to the bacterial cell is facilitated mainly due to the roughness of the surface and contrasting surface charges of bacterium (negative) and transition-metal-doped TiO_2 (positively charged) and inevitably resulting in cell death due to the infiltration of metallic nanomaterials. The above findings have been further validated by Cu−Fe/TiO_2 docking studies at the active site of *E. coli* β-lactamase, with ample proof of TiO_2 invading the active sites, which eventually leads to a higher photobiocidal efficiency.[41,47,54,55] The biochemical pathway of antimicrobial action was clarified by molecular docking since antimicrobial activity can be due to photocatalyst dissolution or direct interaction with microorganisms. Our findings are comparable to those of non-metal-doped TiO_2 (N/TiO_2) in a study carried out by Khan et al., which reported deactivation of the *E. coli* in 120 min;[41] however, Cu−Fe/TiO_2 showed promising inactivation activity in 30 min. In another study, Ag- and N-doped TiO_2 increased the antibacterial properties of TiO_2 nanoparticles under fluorescent light irradiation,[56] which indicates that the combination of metal and nonmetal doped TiO_2 can be studied in the future for best performance.

https://doi.org/10.1021/acsomega.1c03102
ACS Omega 2021, 6, 26108−26118

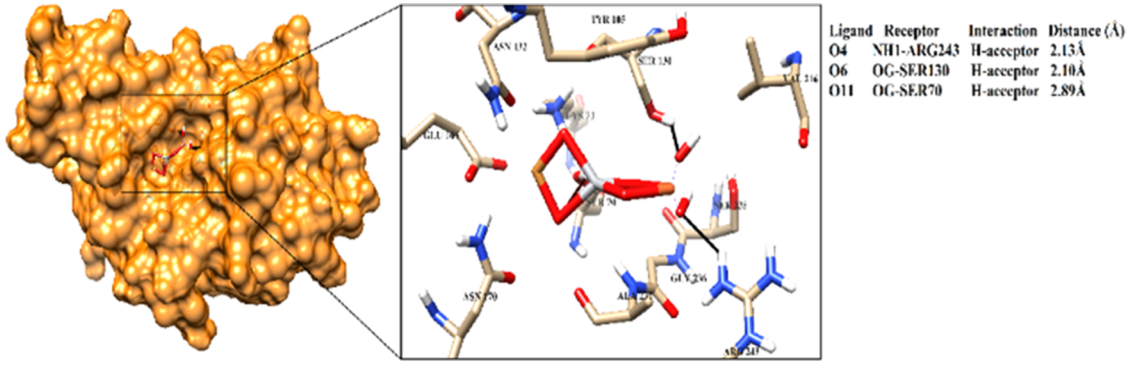

Figure 5. Docked view of the ligand is shown in the active site of *E. coli* β-lactamase. Ligand is shown in red color. Active site residues are depicted in tan color, and hydrogen bonds are shown as black lines. The protein−ligand binding interactions and bond length are shown on the top right side.

Several bacteria produce β-lactamases that break the β-lactam ring of antibiotics, thereby inducing multiple bacterial antibiotic resistance and deactivating antibiotic properties. Since the Cu−Fe/TiO_2 photocatalyst showed excellent bactericidal activity against *E. coli*, the β-lactamase enzyme of *E. coli* was picked as a possible drug target. At the active site of β-lactamase, the Cu−Fe/TiO_2 photocatalyst was identified to be conveniently positioned in the active site and exhibited improved binding activity with the active site residues. The Fe-associated hydroxyl groups of the photocatalyst mediated strong hydrogen bonds with the side chains of (−OH) Ser130 and (NH1) Arg243, while the side chain −OH of Ser70 donated a hydrogen bond to the oxygen linked between Ti and Cu ions. Due to these strong interactions within the active site of the enzyme, the photocatalyst exhibited a high negative docking score (−5.9 kcal mol^{-1}). The binding interactions of the Cu−Fe/TiO_2 photocatalyst within the *E. coli* β-lactamase active site are depicted in Figure 5. These significant protein−ligand binding interactions and high negative docking score indicate that the ligand could inhibit β-lactamase to produce its bactericidal activity.

2.10. Interpretation of Photoactivity. Due to the optimum performance of the 5Cu−5Fe/TiO_2-300 photocatalysts, we focus our characterization study on such sample and, particularly, on understanding the promotion effect of the binary material with respect to single metal references. For this, we first measured the main physicochemical properties in Table 3. In this table, we observed the constancy of the

Table 3. Main Physicochemical Properties of the Photocatalysts[a]

photocatalysts	BET area (m^2 g^{-1})	band gap (eV)
TiO_2	9.0	3.1
T-300	7.6	3.1
0Cu−10Fe-300-T	8.6	3.1
5Cu−5Fe-300-T	8.9	3.1
10Cu−0Fe-300-T	8.7	3.1

[a]Average standard error; BET area; 2.1 m^2 g^{-1}; band gap, 0.03 eV.

Brunauer−Emmett−Teller (BET) surface area and band gap energy. It is also noticeable that the titania support does not change structurally, as evidenced by the identical X-ray diffraction (XRD) patterns presented in Figure 6. The pattern presented corresponds to an anatase structure. The combination of these results indicates that the deposition of the metal

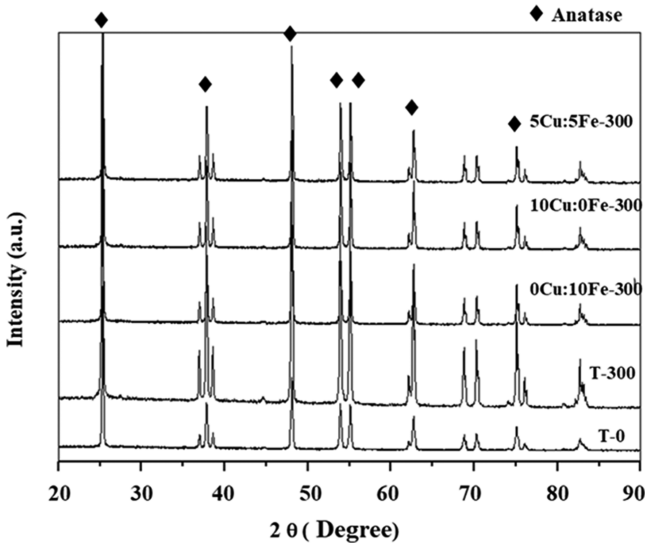

Figure 6. XRD patterns of the samples calcined at 300 °C and references systems.

onto the titania surface does not alter the main structural, morphological, and electronic properties of the support. Concerning the latter, the UV−visible spectra presented in Figure 7 indicate, however, a small increase in light absorption capability of the metal-containing materials with respect to the TiO_2-300, particularly for monometallic reference systems. So, considering the constancy of the physicochemical properties of the titania support through the series of samples, we would thus dismiss any differential effect of the support properties between the Cu and/or Fe photocatalysts and the TiO_2-300 reference. This clearly shows the key role of Cu and Fe in promoting the activity, as previously observed by others.[57−60]

To interpret the important catalytic enhancement presented by 5Cu−5Fe/TiO_2-300 in the bimetallic sample with respect to the monometallic counterparts, we carried out an XPS study of the corresponding samples. Cu and Fe 2p XPS spectra are presented in Figure 8, and fitting results are presented in Table S1. Rather similar spectra are observed between the monometallic and the bimetallic samples.[61] Fe shows a binding energy characteristic of Fe(III), while the shape of the Cu XPS spectra indicates the presence of oxidized Cu(I) and Cu(II) species. The low shake-up intensity, as well as the energy position of the components obtained by fitting (Figure 8), indicates the dominance of a Cu(I) species.[61] According to

https://doi.org/10.1021/acsomega.1c03102
ACS Omega 2021, 6, 26108−26118

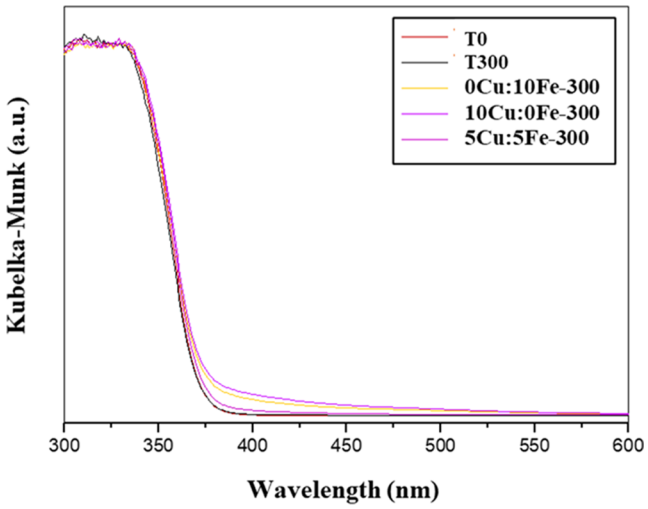

Figure 7. UV−visible spectra of the samples calcined at 300 °C and references systems.

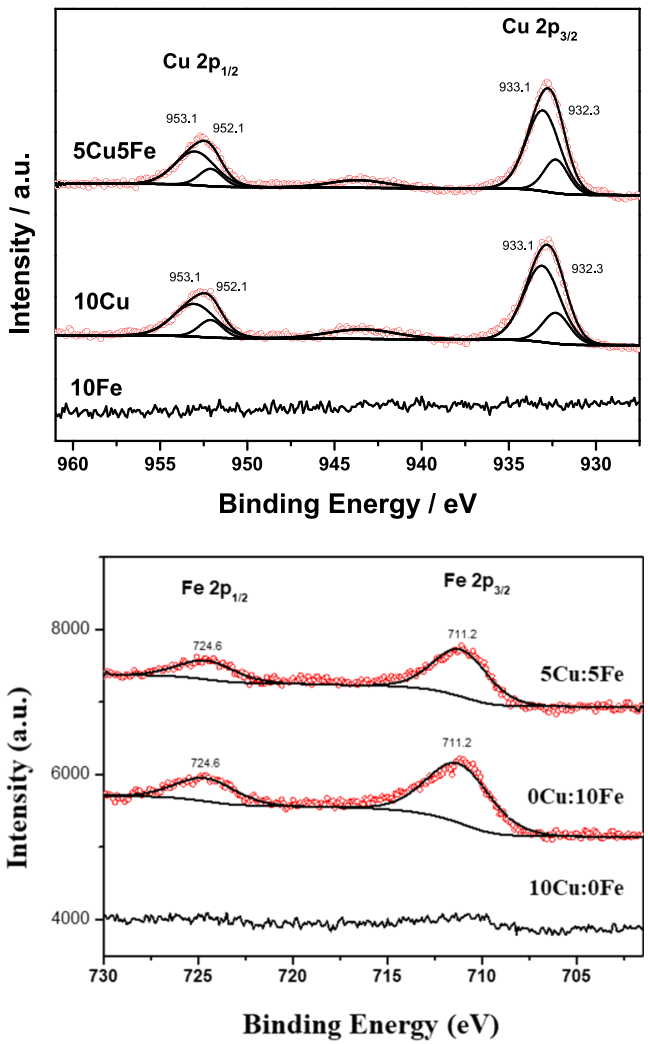

Figure 8. Cu 2p (top panel) and Fe 2p (lower panel) XPS spectra of samples calcined at 300 °C and references systems. Cu panel shows fitting results concerning two chemical species.

XPS and the quantity of the Cu and Fe present in each catalyst, differences between monometallic and bimetallic samples are rather modest and mostly related to a decrease of Fe dispersion in the bimetallic catalysts with respect to the reference. As shown in Figure 8, such changes do not produce an increase in light absorption for the bimetallic material with respect to monometallic counterparts. However, it has a beneficial effect on charge recombination. The Cu−Fe bimetallic catalyst optimizes such function, as indicated by the XPS study. The Cu^{+}−O bond and Cu0 have been created in the TiO_2 lattice, as can be seen on the surface of TiO_2, since XPS detects species primarily on the outer surface or in a very shallow surface layer. Cu/TiO_2 exhibits two sets of peaks, one primary peak at 932.3 eV and the other at 933.1 eV, as illustrated in Figure 8, resulting from Cu^{2+} states generated by Cu oxidation during the XPS test. The broad peak around 932.3 eV could be due to a mixture of Cu^{+} and Cu0 because their binding energies are close and difficult to distinguish.[62,63]

As shown in Figure 9, we have observed the presence of de-excitation peaks at ca. 460 and 520 nm as previously observed

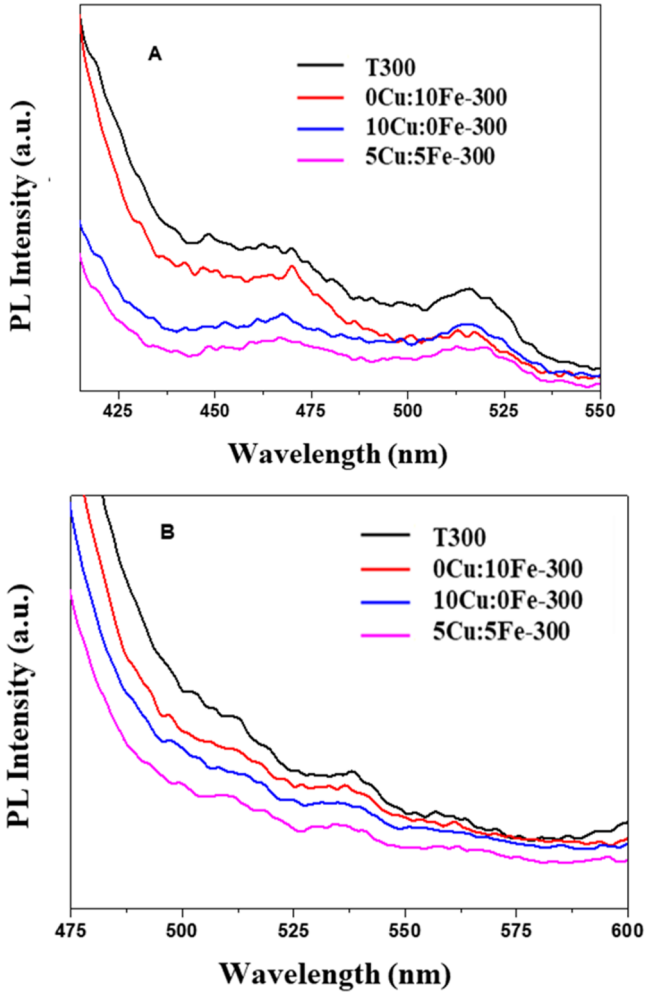

Figure 9. Photoluminescence spectra of the samples: (A) 365 nm and (B) 425 nm excitation.

by others under UV excitation, and very weak contributions at ca. 520 and 540 nm under visible excitation.[64] These contributions are characteristic of anatase and display a rather similar shape for all of our samples. This point indicates that the metal presence does not generate new channels for de-excitation but affects clearly the intensity, thereby decreasing

https://doi.org/10.1021/acsomega.1c03102
ACS Omega 2021, 6, 26108−26118

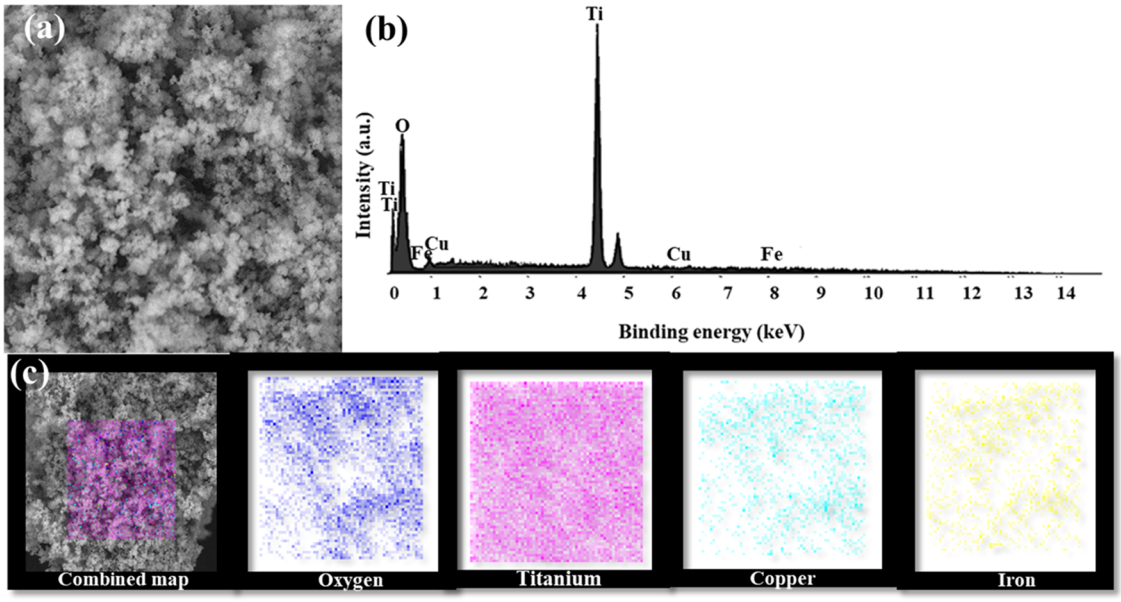

Figure 10. SEM−EDX of the 5Cu−5Fe/TiO_2 samples calcined at 300 °C: (a) morphology, (b) elemental dispersion, and (c) elemental mapping (resolution: 61 × 64 pixels).

charge recombination.[65] The behavior of the photoluminescence intensity is (inversely) proportional to the activity behavior through the series, indicating that the main catalytic effect of the Fe and Cu relates to charge recombination and that the Cu−Fe bimetallic catalyst optimizes such function.

The morphology and elemental distribution of photocatalysts were analyzed using scanning electron microscopy-energy-dispersive X-ray analysis (SEM−EDX). It can be seen in Figure 10a that photocatalyst particles were spherical and agglomerated. A clearer picture of the elemental dispersion along with the elemental mapping can be seen in Figure 10b,c.

3. SUMMARY AND CONCLUSIONS

Cu−Fe/TiO_2 photocatalysts were synthesized through the WI method. Synthesis parameters were optimized for the Cu-to-Fe ratio, metal loading, and calcination temperatures. Photocatalysts with 1 wt % 5Cu−5Fe/TiO_2 showed the maximum MO decolorization (97.1%) in 60 min. Various parameters like photocatalyst dose, dye concentration, and irradiation time were monitored to validate the photocatalyst performance. Mineralization studies and COD/TO-carbon analysis clearly demonstrated that synthesized photocatalysts were capable of completely degrading the MO dye. The dependence of the initial degradation rate on the MO_o concentration followed the Langmuir−Hinshelwood (L−H) model, indicating that photocatalysts have a high adsorption capacity, which in turn has enhanced the photocatalytic performance. The photocatalytic performance of Cu−Fe/TiO_2 was attributed to the high photogenerated electron−hole separation efficiency. Additional bactericidal activity testing was performed to verify the photocatalytic disinfection capacity of the best-performing photocatalyst against various parameters, including irradiation time (kill time) and calcination temperatures. The 5Cu−5Fe/TiO_2-300 photocatalyst showed a much-improved efficiency for maximum % reduction of *E. coli* in 30 min of irradiation under visible light. The biocidal mechanism was explained by docking simulation, which demonstrated that the Cu−Fe/TiO_2 photocatalyst might impact this activity by inhibiting the β-lactamase enzymes with a high negative docking score (−5.9 kcal mol^{-1}). Moreover, the BET surface area and band gap energy were found to be consistent, and the XRD patterns reported corresponded to an anatase structure. The primary structural, morphological, and electrical features of the support are unaffected by the metal deposition on the titania surface. However, as compared to TiO_2-300, the metal-containing compounds showed a slight increase in light absorption capabilities.

4. METHODOLOGY

4.1. Materials. Metal salts used as dopant metals were copper nitrate trihydrate, $Cu(NO_3)_2{\cdot}3H_2O$, (Dae-Jung brand > 99.0% purity) and iron nitrate nonahydrate $Fe(NO_3)_3{\cdot}9H_2O$ (Dae-Jung brand > 97.0% purity). Titanium dioxide (TiO_2, Anatase) was used as the support and was purchased from Dae-Jung with 98.0% purity. Methyl orange, the model azo dye, was purchased from Fluka. All of the chemicals were used without any further purification.

4.2. Photocatalyst Preparation. A range of bimetallic photocatalysts were synthesized with varying mass compositions (Cu/Fe) employing TiO_2 as the support via the WI method reported in our previous publication.[48] In a typical method, to synthesize 1 wt % Cu/Fe photocatalysts, 7.87 × 10^{-4} moles of $Cu(NO_3)_2{\cdot}3H_2O$ and 8.95 × 10^{-4} moles of $Fe(NO_3)_3{\cdot}9H_2O$ were stirred (stirring hotplate, DLAB MS7 H550-S, Riverside, CA) in 100 mL of deionized water to obtain a homogeneous solution, where after 1.25 × 10^{-1} moles of TiO_2 was introduced under continuous stirring into this homogeneous solution to form a slurry. A thick paste was obtained upon heating the slurry. This thick paste was kept overnight to age, followed by drying in an oven (UN 30, Memmert-Kupfer, Dominik, Germany). The raw photocatalyst (dried paste) was ground into powder and calcined at different calcination temperatures. The denotation of the synthesized photocatalyst is explained in the Supporting Information (Scheme S1), and the flow diagram of the wet impregnation synthesis is given in the Supporting Information (Figure S2).

4.3. Photocatalytic Degradation and Mineralization Study. Photocatalytic decolorization efficiency of the synthe-

https://doi.org/10.1021/acsomega.1c03102
ACS Omega 2021, 6, 26108−26118

sized material was assessed through percent decolorization of MO under visible light irradiation. An appropriate amount of photocatalysts was ultrasonically (ultrasonicator, FSF-020S Huanghua Faithful Instrument, Huanghua, China) dispersed in water for 10 min, followed by the addition of the desired amount of MO with a final concentration of 50 mg L^{-1}. This heterogeneous mixture was stirred for 30 min in dark and then illuminated under visible light (500 W halogen lamp, Hi Luminar, Bayern, Germany) at 25 cm. The samples were drawn from the heterogeneous mixture at a predetermined time interval to check the absorbance through UV−vis spectrophotometer (PG instrument, T80+ series) at 465 nm wavelength. Prior to absorbance measurement for the residual MO concentration, the samples were centrifuged to remove the suspended photocatalysts.

The photodecoloration efficiency of the photocatalyst was determined using eq 1

$$\text{MO photodecoloration (\%)} = \left(\frac{C_0 - C_f}{C_0}\right) \times 100 \quad (1)$$

where C_0 is the initial MO concentration (mg L^{-1}) and C_f is the MO concentration (mg L^{-1}) at different intervals of time during the reaction.

Mineralization studies of MO after irradiation were monitored in terms of % COD and % TO-carbon removal using AL100, AQUALYTIC, as the chemical oxygen demand (COD) and TOC removal according to eqs 2 and 3.

$$\text{COD removal (\%)} = \left(\frac{\text{COD}_0 - \text{COD}_f}{\text{COD}_0}\right) \times 100 \quad (2)$$

$$\text{TO} - \text{carbon removal (\%)} = \left(\frac{\text{TO} - \text{carbon}_0 - \text{TO} - \text{carbon}_f}{\text{TOC}_0}\right) \times 100 \quad (3)$$

where COD_0 or TO-carbon_0 is initial MO COD/TO-carbon (mg L^{-1}) and COD_f or TO-carbon_f is the MO COD/TO-carbon concentration (mg L^{-1}) at different intervals of time during the reaction.

4.3.1. Optimization of Synthesis Parameters. Synthesis parameters were optimized for the selection of best suitable synthesis combinations for Cu−Fe/TiO_2 photocatalysts. These included (a) selection of best Cu and Fe mass composition (10:0, 9:1, 7:3, 5:5, 3:7, 1:9, 0:10), (b) selection of metal loading (wt %), i.e., 0.5, 1, 5, and 10, and (c) selection of a suitable calcination temperature, i.e., 300 and 500 °C.

4.3.2. Optimization of Reaction Parameters. Optimization of reaction parameters is crucial in terms of the economic and energy value of the heterogeneous system. The best-optimized photocatalyst, 5Cu−5Fe/TiO_2-300 with 1% metal loading, was further used to optimize the reaction parameters. These reaction parameters include (a) photocatalyst dose, (b) irradiation time, and (c) initial MO concentration.

4.4. Photocatalytic Bactericidal Performance Evaluation and Molecular Docking Studies. The photocatalytic disinfection ability of the best-performing nanomaterial was further tested for bactericidal activity against *E. coli* (ATCC-15224)[66] following the bactericidal activity protocol explained elsewhere.[41,42,47] The media and glassware were autoclaved before the experiment. For a classic photocatalytic reaction for bacterial inactivation, known amounts of mature bacterial culture (10^4 CFU mL^{-1}) were transferred to freshly prepared autoclaved broth cultures in a glass vessel, followed by the addition of the desired amount of photocatalysts (1 g L^{-1}). All of the disinfection studies (180 min) were carried out in a photoreaction chamber (placed inside a laminar flow hood) under a visible light source. Specified amounts of aliquots (at fixed time) were extracted and poured on agar plates, followed by incubation (at 37 °C) and analysis of results (utilizing a colony counter).

Controlled tests were also performed in dark and light using TiO_2-300 and without photocatalyst. Findings are presented as % reduction pre- and post-photocatalytic oxidation process (PCO) using the given eqs 4 and 5.

$$\text{percent reduction} = \left(\frac{A - B}{A}\right) \times 100 \quad (4)$$

where A is the count for the bacterial cells prior to PCO and B is the count of the viable bacterial cells following PCO.

The inactivation efficiency[67] of the nanomaterials was shown by log unit reduction of *E. coli* (L_r)

$$\text{log unit reduction of } E.\ coli\ (L_r): = \frac{A_t}{A_0} \quad (5)$$

where A_t and A_0 are the initial concentration and the concentration at a particular irradiation time during photocatalytic inactivation experiments, respectively.

An *in silico* structure-based docking strategy was applied to investigate the mechanism of the bactericidal activity of Cu−Fe/TiO_2. Molecular Operating Environment (MOE version 2014.09) was used to carry out docking on the three-dimensional X-ray crystal structure of *E. coli* β-lactamase (PDB ID: 1ERM,[68] resolution = 1.70 Å). The protein file was prepared for docking by adding hydrogen atoms and partial charges (according to the AMBER12:EHT force field). Only water molecules within the 3 Å vicinity of the active site were retained, while the rest were removed. The three-dimensional (3D) structure of Cu−Fe/TiO_2 was built on MOE using the AMBER12:EHT force field with the given parameters for Cu (mass = 63.5460, q = 0.000, R = 1.7475, E_{ps} = 0.0707, m = 12, and n = 6), Fe (mass = 55.8500, q = −2.00, R = 1.200, E_{ps} = 0.0500, m = 12, and n = 6), and Ti (mass = 47.8670, q = −2.00, R = 1.5875, E_{ps} = 0.1304, m = 12, and n = 6). The docking was performed with the default docking algorithm and scoring function (triangle matcher algorithm and London dG). Several docked conformations of ligand were obtained that were individually visualized. The most appropriate docked orientation was selected based on the docking score and binding interactions.

4.5. Photocatalytic Kinetic Studies. Kinetic studies were conducted with different kinetic equations and the data best fitted to the pseudo-first-order (PFO) kinetic model (eq 6)

$$\ln \frac{[C_0]}{[C_t]} = K_{app}t \quad (6)$$

The rate of decolorization of the MO dye using 5Cu−5Fe/TiO_2-300 in a heterogeneous system was assessed through the Langmuir−Hinshelwood (LH) isotherm. The LH expression is given in eq 7

$$r_0 = \frac{\text{dMO}}{\text{d}t} = \frac{k_c K_{ads}\text{MO}}{1 + K_{ads}\text{MO}} \quad (7)$$

https://doi.org/10.1021/acsomega.1c03102
ACS Omega 2021, 6, 26108−26118

where dMO is the change in MO concentration, dt is the change in time (min), k_c is the rate constant, K_{ads} is the adsorption coefficient, and MO is the MO concentration.

4.6. Characterization Studies. The synthesized material was characterized using different analysis tools. To understand the surface area and pore volumes, the samples were analyzed by nitrogen physisorption using BET analysis (Micromeritics ASAP 2010). XRD profiles were obtained using a Ni-filtered Cu Kα radiation with a 0.02° step (Seifert D-500 diffractometer). XRD was also used to determine crystallite sizes of photocatalysts (Williamson−Hall formalism).[69] Shimadzu UV2100 apparatus was used to determine UV−vis diffuse-reflectance (nylon was used as a reference sample), and the results were presented as Kubelka−Munk transform.[70] The chemical, electronic state, and elemental composition of doped metals into the TiO_2 was studied using X-ray photoelectron spectroscopy (XPS) by recording data on 4 × 4 mm^2 pellets (0.5 mm thick). Powdered materials were slightly pressed for the preparation of pellets. To remove chemisorbed water from surfaces, the samples were degassed at room temperature (up to a pressure <2 × 10^{-8} Torr) in the prechamber of the instrument. The SPECS spectrometer main chamber (working at a pressure <10^{-9} Torr) was furnished with a PHOIBOS 150 multichannel hemispherical electron analyzer with a dual X-ray source working with Ag Kα ($h\nu$ = 1486.2 eV) at 120 W and 20 mA using C 1s as the energy reference (284.6 eV). Surface chemical compositions from XPS spectra were assessed by calculating the integral of each peak after subtraction of the "S-shaped" Shirley-type background[71] using CASA-XPS (version 2.3.15) software and suitable experimental sensitivity factors. JEOL JSM-6510LA was used to understand the surface morphologies of the synthesized photocatalysts.

■ ASSOCIATED CONTENT

Supporting Information

The Supporting Information is available free of charge at https://pubs.acs.org/doi/10.1021/acsomega.1c03102.

(a) Pseudo-first-order and (b) second-order kinetic fitness of 5Cu−5Fe-TiO_2-300 for different initial MO concentrations; information about binding energies of the elements in the synthesized photocatalyst (Figure S1); XPS binding energies (eV) and atomic ratios and the denotation of the synthesized photocatalyst (Table S1); and denotation of the synthesized photocatalysts (Scheme S1) (PDF)

■ AUTHOR INFORMATION

Corresponding Authors

Nadia Riaz − *Department of Environmental Sciences, COMSATS University Islamabad, Abbottabad 22060, Pakistan*; orcid.org/0000-0002-0931-1089; Email: nadiariazz@gmail.com

Marcos Fernández García − *Instituto de Catálisis y Petroleoquímica, CSIC, Madrid 28049, Spain*; Email: mfg@icp.csic.es

Ajmal Khan − *Natural and Medical Sciences Research Center, University of Nizwa, Nizwa 616, Sultanate of Oman*; Email: ajmalkhan@unizwa.edu.om

Ahmed Al-Harrasi − *Natural and Medical Sciences Research Center, University of Nizwa, Nizwa 616, Sultanate of Oman*; orcid.org/0000-0002-0815-5942; Email: aharrasi@unizwa.edu.om

Authors

Muhammad Saqib Khan − *Department of Environmental Sciences, COMSATS University Islamabad, Abbottabad 22060, Pakistan*; orcid.org/0000-0002-0897-7436

Mehraj Javed − *Department of Environmental Sciences, COMSATS University Islamabad, Abbottabad 22060, Pakistan*

Anna Kubacka − *Instituto de Catálisis y Petroleoquímica, CSIC, Madrid 28049, Spain*

Uriel Caudillo-Flores − *Instituto de Catálisis y Petroleoquímica, CSIC, Madrid 28049, Spain*

Sobia Ahsan Halim − *Natural and Medical Sciences Research Center, University of Nizwa, Nizwa 616, Sultanate of Oman*

Complete contact information is available at: https://pubs.acs.org/10.1021/acsomega.1c03102

Author Contributions

The manuscript was written through the contributions of all authors. All authors have given approval to the final version of the manuscript.

Funding

The project was supported by a grant from The Oman Research Council (TRC) through the funded project (BFP/RGP/CBS/19/220).

Notes

The authors declare no competing financial interest.

■ ACKNOWLEDGMENTS

The authors acknowledge the Instituto de Catálisis y Petroleoquímica, CSIC, C/Marie Curie, 2, 28049, Madrid, Spain, for characterization and analysis of some of our research samples used in this study.

■ REFERENCES

(1) Alheety, M. A.; Raoof, A.; Al-Jibori, S. A.; Karadağ, A.; Khaleel, A. I.; Akbaş, H.; Uzun, O. Eco-friendly C60-SESMP-Fe3O4 inorganic magnetizable nanocomposite as high-performance adsorbent for magnetic removal of arsenic from crude oil and water samples. *Mater. Chem. Phys.* **2019**, *231*, 292−300.

(2) Lartiges, S. B.; Garrigues, P. P. Degradation Kinetics of Organophosphorus and Organonitrogen Pesticides in Different Waters under Various Environmental Conditions. *Environ. Sci. Technol.* **1995**, *29*, 1246−1254.

(3) Vandevivere, P. C.; Bianchi, R.; Verstraete, W. Treatment and reuse of wastewater from the textile wet-processing industry: Review of emerging technologies. *J. Chem. Technol. Biotechnol.* **1998**, *72*, 289−302.

(4) Aljerf, L. High-efficiency extraction of bromocresol purple dye and heavy metals as chromium from industrial effluent by adsorption onto a modified surface of zeolite: kinetics and equilibrium study. *J. Environ. Manage.* **2018**, *225*, 120−132.

(5) Akther, S.; Debnath, T.; Chowdhury, M. M. H. Multidrug Resistant E. coli in hospital waste water: a potential concern for public health. *Adv. Biotechnol. Microbiol.* **2018**, *8*, No. 555729.

(6) Gaya, U. I.; Abdullah, A. H. Heterogeneous photocatalytic degradation of organic contaminants over titanium dioxide: a review of fundamentals, progress and problems. *J. Photochem. Photobiol., C* **2008**, *9*, 1−12.

(7) Nakata, K.; Fujishima, A. TiO2 photocatalysis: Design and applications. *J. Photochem. Photobiol., C* **2012**, *13*, 169−189.

(8) Etacheri, V.; Di Valentin, C.; Schneider, J.; Bahnemann, D.; Pillai, S. C. Visible-light activation of TiO2 photocatalysts: Advances in theory and experiments. *J. Photochem. Photobiol., C* **2015**, *25*, 1−29.

(9) Zhang, X.; Wang, Y.; Li, G. Effect of operating parameters on microwave assisted photocatalytic degradation of azo dye X-3B with grain TiO2 catalyst. *J. Mol. Catal. A: Chem.* **2005**, *237*, 199−205.
(10) Chen, H.; Wu, T.; Li, X.; Lu, S.; Zhang, F.; Wang, Y.; Zhao, H.; Liu, Q.; Luo, Y.; Asiri, A. M. Modulating Oxygen Vacancies of TiO2 Nanospheres by Mn-Doping to Boost Electrocatalytic N2 Reduction. *ACS Sustainable Chem. Eng.* **2021**, *9*, 1512−1517.
(11) Khairy, M.; Zakaria, W. Effect of metal-doping of TiO2 nanoparticles on their photocatalytic activities toward removal of organic dyes. *Egypt. J. Pet.* **2014**, *23*, 419−426.
(12) He, H. Y.; Chen, P. Recent Advances in Property Enhancement of Nano TiO2 In Photodegradation of Organic Pollutants. *Chem. Eng. Commun.* **2012**, *199*, 1543−1574.
(13) Kohtani, S.; Kawashima, A.; Miyabe, H. Reactivity of trapped and accumulated electrons in titanium dioxide photocatalysis. *Catalysts* **2017**, *7*, No. 303.
(14) Hoffmann, M. R.; Martin, S. T.; Choi, W.; Bahnemann, D. W. Environmental applications of semiconductor photocatalysis. *Chem. Rev.* **1995**, *95*, 69−96.
(15) Piera, E.; Tejedor-Tejedor, M. I.; Zorn, M. E.; Anderson, M. A. Relationship concerning the nature and concentration of Fe(III) species on the surface of TiO2 particles and photocatalytic activity of the catalyst. *Appl. Catal., B* **2003**, *46*, 671−685.
(16) Ikram, M.; Umar, E.; Raza, A.; Haider, A.; Naz, S.; Ul-Hamid, A.; Haider, J.; Shahzadi, I.; Hassan, J.; Ali, S. Dye degradation performance, bactericidal behavior and molecular docking analysis of Cu-doped TiO2 nanoparticles. *RSC Adv.* **2020**, *10*, 24215−24233.
(17) Khan, M. S.; Shah, J. A.; Arshad, M.; Halim, S. A.; Khan, A.; Shaikh, A. J.; Riaz, N.; Khan, A. J.; Arfan, M.; Shahid, M. Photocatalytic Decolorization and Biocidal Applications of Nonmetal Doped TiO2: Isotherm, Kinetic Modeling and In Silico Molecular Docking Studies. *Molecules* **2020**, *25*, No. 4468.
(18) Ikram, M.; Aslam, S.; Haider, A.; Naz, S.; Ul-Hamid, A.; Shahzadi, A.; Ikram, M.; Haider, J.; Ahmad, S. O. A.; Butt, A. R. Doping of Mg on ZnO Nanorods Demonstrated Improved Photocatalytic Degradation and Antimicrobial Potential with Molecular Docking Analysis. *Nanoscale Res. Lett.* **2021**, *16*, No. 78.
(19) Zhu, J.; Zheng, W.; He, B.; Zhang, J.; Anpo, M. Characterization of Fe−TiO 2 photocatalysts synthesized by hydrothermal method and their photocatalytic reactivity for photodegradation of XRG dye diluted in water. *J. Mol. Catal. A: Chem.* **2004**, *216*, 35−43.
(20) Anwar, D. I.; Mulyadi, D. Synthesis of Fe-TiO2 Composite as a Photocatalyst for Degradation of Methylene Blue. *Procedia Chem.* **2015**, *17*, 49−54.
(21) Hung, W.-C.; Chen, Y.-C.; Chu, H.; Tseng, T.-K. Synthesis and characterization of TiO2 and Fe/TiO2 nanoparticles and their performance for photocatalytic degradation of 1, 2-dichloroethane. *Appl. Surf. Sci.* **2008**, *255*, 2205−2213.
(22) Zhang, W.; Chen, Y.; Yu, S.; Chen, S.; Yin, Y. Preparation and antibacterial behavior of Fe3+-doped nanostructured TiO2 thin films. *Thin Solid Films* **2008**, *516*, 4690−4694.
(23) Al-Jawad, S. M. H.; Taha, A. A.; Salim, M. M. Synthesis and characterization of pure and Fe doped TiO2 thin films for antimicrobial activity. *Optik* **2017**, *142*, 42−53.
(24) Mathew, S.; Ganguly, P.; Rhatigan, S.; Kumaravel, V.; Byrne, C.; Hinder, S.; Bartlett, J.; Nolan, M.; Pillai, S. Cu-doped TiO2: visible light assisted photocatalytic antimicrobial activity. *Appl. Sci.* **2018**, *8*, No. 2067.
(25) Riaz, N.; Kait, C. F.; Man, Z.; Dutta, B. K.; Ramli, R. M.; Khan, M. S. Visible Light Photodegradation of Azo Dye by Cu/TiO_2. In *Advanced Materials Research*; Trans Tech Publication, 2014; pp 151−159.
(26) Riaz, N.; Bustam, M. A.; Chong, F. K.; Man, Z. B.; Khan, M. S.; Shariff, A. M. Photocatalytic Degradation of DIPA Using Bimetallic Cu-Ni/TiO2 Photocatalyst under Visible Light Irradiation. *Sci. World J.* **2014**, *2014*, No. 342020.
(27) Zaid, H. F. M.; Chong, F. K.; Abdul Mutalib, M. I. Preparation and characterization of Cu−Fe/TiO2 photocatalyst for visible light deep desulfurization. *Malays. J. Anal. Sci.* **2016**, *20*, 713−725.
(28) Zaid, H. F. M.; Chong, F. K.; Mutalib, M. I. A. Photooxidative−extractive deep desulfurization of diesel using Cu−Fe/TiO 2 and eutectic ionic liquid. *Fuel* **2015**, *156*, 54−62.
(29) Riaz, N.; Chong, F.; Man, Z.; Sarwar, R.; Farooq, U.; Khan, A.; Khan, M. Preparation, characterization and application of Cu−Ni/TiO2 in Orange II photodegradation under visible light: effect of different reaction parameters and optimization. *RSC Adv.* **2016**, *6*, 55650−55665.
(30) Riaz, N.; Chong, F. K.; Dutta, B. K.; Man, Z. B.; Khan, M. S.; Nurlaela, E. Photodegradation of Orange II under visible light using Cu−Ni/TiO2: Effect of calcination temperature. *Chem. Eng. J.* **2012**, *185−186*, 108−119.
(31) Riaz, N.; Chong, F. K.; Man, Z. B.; Khan, M. S.; Dutta, B. K. Photodegradation of Orange II under Visible Light Using Cu−Ni/TiO2: Influence of Cu:Ni Mass Composition, Preparation, and Calcination Temperature. *Ind. Eng. Chem. Res.* **2013**, *52*, 4491−4503.
(32) Saraswat, S. K.; Sinha, B.; Pant, K.; Gupta, R. B. Kinetic Study and Modeling of Homogeneous Thermocatalytic Decomposition of Methane over a Ni−Cu−Zn/Al2O3 Catalyst for the Production of Hydrogen and Bamboo-Shaped Carbon Nanotubes. *Ind. Eng. Chem. Res.* **2016**, *55*, 11672−11680.
(33) Bashiri, R.; Mohamed, N. M.; Kait, C. F.; Sufian, S.; Khatani, M. Enhanced hydrogen production over incorporated Cu and Ni into titania photocatalyst in glycerol-based photoelectrochemical cell: Effect of total metal loading and calcination temperature. *Int. J. Hydrogen Energy* **2017**, *42*, 9553−9566.
(34) Pradhan, A. C.; Martha, S.; Mahanta, S.; Parida, K. Mesoporous nanocomposite Fe/Al2O3−MCM-41: An efficient photocatalyst for hydrogen production under visible light. *Int. J. Hydrogen Energy* **2011**, *36*, 12753−12760.
(35) Van Slyke, D. D.; Palmer, W. *Studies of Acidosis*; Rockefeller Institute for Medical Research, 1921; Vol. *36*, p 377.
(36) Castañeda-Juárez, M.; Martínez-Miranda, V.; Almazán-Sánchez, P. T.; Linares-Hernández, I.; Santoyo-Tepole, F.; Vázquez-Mejía, G. Synthesis of TiO2 catalysts doped with Cu, Fe, and Fe/Cu supported on clinoptilolite zeolite by an electrochemical-thermal method for the degradation of diclofenac by heterogeneous photocatalysis. *J. Photochem. Photobiol., A* **2019**, *380*, No. 111834.
(37) Riaz, N.; Chong, F. K.; Dutta, B. K.; Man, Z. B.; Khan, M. S.; Ramli, R. M. In *Azo Dye Degradation Using Cu/TiO2 Under Visible Light: Effect of Metal Loading*, 2nd International Conference on Process Engineering and Advanced Materials (ICPEAM); IEEE: Kulala Lumpur, 2012; p 6.
(38) Yin, R.; Ling, L.; Lu, S.; Li, H.; Li, C.; Shang, C. Degradation of aliphatic halogenated contaminants in water by UVA/Cu−TiO2 and UVA/TiO2 photocatalytic processes: Structure-activity relationship and role of reactive species. *Chemosphere* **2020**, *260*, No. 127644.
(39) Cai, J.; Xin, W.; Liu, G.; Lin, D.; Zhu, D. Effect of calcination temperature on structural properties and photocatalytic activity of Mn-C-codoped TiO2. *Mater. Res.* **2016**, *19*, 401−407.
(40) Riaz, N.; Chong, F. K.; Dutta, B. K.; Man, Z. B.; Khan, M. S.; Nurlaela, E. In *Effect of Calcination Temperature on Orange II Photocatalytic Degradation Using Cu:Ni/TiO2 under Visible Light*, 2011 National Postgraduate Conference, 19−20 September, 2011; pp 1−5.
(41) Khan, M. S.; Shah, J. A.; Arshad, M.; Halim, S. A.; Khan, A.; Shaikh, A. J.; Riaz, N.; Khan, A. J.; Arfan, M.; Shahid, M.; Pervez, A.; Harasi, A.; Bilal, M. Photocatalytic decolorization and biocidal applications of nonmetal doped TiO2: Isotherm, kinetic modeling and In Silico molecular docking studies. *Molecules* **2020**, *25*, No. 4468.
(42) Khan, M. S.; Shah, J. A.; Riaz, N.; Butt, T. A.; Khan, A. J.; Khalifa, W.; Gasmi, H. H.; Latifee, E. R.; Arshad, M.; Al-Naghi, A. A. A.; Ul-Hamid, A.; Arshad, M.; Bilal, M. Synthesis and Characterization of Fe-TiO2 Nanomaterial: Performance Evaluation for RB5 Decolorization and In Vitro Antibacterial Studies. *Nanomaterials* **2021**, *11*, No. 436.
(43) Khan, M. S.; Kait, C. F.; Mutalib, M. I. A. In *Photooxidative desulfurization for diesel using Fe/N−TiO2 photocatalyst*, AIP Conference Proceedings, Kaula Lumpur; American Institute of Physics Publishing LLC: College Park, MD, USA, 2014; pp 1−8.

https://doi.org/10.1021/acsomega.1c03102
ACS Omega 2021, 6, 26108−26118

(44) Nechifor, G.; Totu, E. E.; Nechifor, A. C.; Constantin, L.; Constantin, A. M.; Cărăuşu, M. E.; Isildak, I. Added value recyclability of glass fiber waste as photo-oxidation catalyst for toxic cytostatic micropollutants. *Sci. Rep.* **2020**, *10*, No. 136.
(45) Lathasree, S.; Rao, A. N.; SivaSankar, B.; Sadasivam, V.; Rengaraj, K. Heterogeneous photocatalytic mineralisation of phenols in aqueous solutions. *J. Mol. Catal. A: Chem.* **2004**, *223*, 101−105.
(46) Yang, H.; Zhang, K.; Shi, R.; Li, X.; Dong, X.; Yu, Y. Sol−gel synthesis of TiO2 nanoparticles and photocatalytic degradation of methyl orange in aqueous TiO2 suspensions. *J. Alloys Compd.* **2006**, *413*, 302−306.
(47) Iftikhar, A.; Khan, M. S.; Rashid, U.; Mahmood, Q.; Zafar, H.; Bilal, M.; Riaz, N. Influence of metallic species for efficient photocatalytic water disinfection: bactericidal mechanism of in vitro results using docking simulation. *Environ. Sci. Pollut. Res.* **2020**, *27*, 39819−39831.
(48) Riaz, N.; Hassan, M.; Siddique, M.; Mahmood, Q.; Farooq, U.; Sarwar, R.; Khan, M. S. Photocatalytic degradation and kinetic modeling of azo dye using bimetallic photocatalysts: effect of synthesis and operational parameters. *Environ. Sci. Pollut. Res.* **2020**, *27*, 2992−3006.
(49) Kumar, K. V.; Porkodi, K.; Rocha, F. Langmuir−Hinshelwood kinetics—A theoretical study. *Catal. Commun.* **2008**, *9*, 82−84.
(50) Albrbar, A. J.; Bjelajac, A.; Đokić, V.; Miladinović, J.; Janaćković, Đ.; Petrović, R. Photocatalytic efficiency of titania photocatalysts in saline waters. *J. Serb. Chem. Soc.* **2014**, *79*, 1127−1140.
(51) Hernández, R.; Olvera-Rodríguez, I.; Guzmán, C.; Medel, A.; Escobar-Alarcón, L.; Brillas, E.; Sirés, I.; Esquivel, K. Microwave-assisted sol-gel synthesis of an Au-TiO2 photoanode for the advanced oxidation of paracetamol as model pharmaceutical pollutant. *Electrochem. Commun.* **2018**, *96*, 42−46.
(52) Delsouz Khaki, M. R.; Shafeeyan, M. S.; Raman, A. A. A.; Daud, W. M. A. W. Evaluating the efficiency of nano-sized Cu doped TiO2/ZnO photocatalyst under visible light irradiation. *J. Mol. Liq.* **2018**, *258*, 354−365.
(53) Talebian, N.; Nilforoushan, M. R.; Zargar, E. B. Enhanced antibacterial performance of hybrid semiconductor nanomaterials: ZnO/SnO2 nanocomposite thin films. *Appl. Surf. Sci.* **2011**, *258*, 547−555.
(54) Grace, J. L.; Huang, J. X.; Cheah, S.-E.; Truong, N. P.; Cooper, M. A.; Li, J.; Davis, T. P.; Quinn, J. F.; Velkov, T.; Whittaker, M. R. Antibacterial low molecular weight cationic polymers: dissecting the contribution of hydrophobicity, chain length and charge to activity. *RSC Adv.* **2016**, *6*, 15469−15477.
(55) Sur, V. P.; Kominkova, M.; Buchtova, Z.; Dolezelikova, K.; Zitka, O.; Moulick, A. CdSe QD Biosynthesis in Yeast Using Tryptone-Enriched Media and Their Conjugation with a Peptide Hecate for Bacterial Detection and Killing. *Nanomaterials* **2019**, *9*, No. 1463.
(56) Yuan, Y.; Ding, J.; Xu, J.; Deng, J.; Guo, J. TiO2 nanoparticles co-doped with silver and nitrogen for antibacterial application. *J. Nanosci. Nanotechnol.* **2010**, *10*, 4868−4874.
(57) Apiwong-ngarm, K.; Pongwan, P.; Inceesungvorn, B.; Phanichphant, S.; Wetchakun, K.; Wetchakun, N. Photocatalytic activities of Fe−Cu/TiO2 on the mineralization of oxalic acid and formic acid under visible light irradiation. *Powder Technol.* **2014**, *266*, 447−455.
(58) Barakat, N. A. M.; Motlak, M.; Taha, A.; Nassar, M. M.; Mahmoud, M. S.; Fouad, H. Super effective Zn-Fe-doped TiO2 nanofibers as photocatalyst for ammonia borane hydrolysis. *Int. J. Green Energy* **2016**, *13*, 642−649.
(59) Roselin, L. S.; AlYoubi, M. M. M.; Mousa, S. M.; El-Komy, G. M.; Patel, N.; Albeladi, N. M.; Selvin, R. Transformation of Commercial TiO2 into Anatase with Improved Activity of Fe, Cu and Cu−Fe Oxides Loaded TiO2. *J. Nanosci. Nanotechnol.* **2019**, *19*, 1098−1104.
(60) Zaid, H. F. M.; Kait, C. F.; Mutalib, M. I. A. Preparation and characterization of Cu−Fe/TiO2 photocatalyst for visible light deep desulfurization. *Malays. J. Anal. Sci.* **2016**, *20*, 713−725.
(61) Wagner, C. D.; Muilenberg, G. E. *Handbook of X-ray Photoelectron Spectroscopy: A Reference Book of Standard Data for Use in X-ray Photoelectron Spectroscopy*; Physical Electronics Division, Perkin-Elmer Corp.: Eden Prairie, Minnesota, 1979.
(62) Zhu, S.; Chen, X.; Li, Z.; Ye, X.; Liu, Y.; Chen, Y.; Yang, L.; Chen, M.; Zhang, D.; Li, G.; Li, H. Cooperation between inside and outside of TiO2: Lattice Cu+ accelerates carrier migration to the surface of metal copper for photocatalytic CO2 reduction. *Appl. Catal., B* **2020**, *264*, No. 118515.
(63) Li, G.; Wang, B.-D.; Sun, Q.; Xu, W.-Q.; Han, Y.-F. Visible-Light Photocatalytic Activity of Fe and/or Ni Doped Ilmenite Derived-Titanium Dioxide Nanoparticles. *J. Nanosci. Nanotechnol.* **2019**, *19*, 3343−3355.
(64) Mercado, C.; Seeley, Z.; Bandyopadhyay, A.; Bose, S.; McHale, J. L. Photoluminescence of Dense Nanocrystalline Titanium Dioxide Thin Films: Effect of Doping and Thickness and Relation to Gas Sensing. *ACS Appl. Mater. Interfaces* **2011**, *3*, 2281−2288.
(65) Aljerf, L.; Nadra, R. Developed greener method based on MW implementation in manufacturing CNFs. *Int. J. Nanomanuf.* **2019**, *15*, 269−289.
(66) Mushtaq, S.; Khan, J. A.; Rabbani, F.; Latif, U.; Arfan, M.; Yameen, M. A. Biocompatible biodegradable polymeric antibacterial nanoparticles for enhancing the effects of a third-generation cephalosporin against resistant bacteria. *J. Med. Microbiol.* **2017**, *66*, 318−327.
(67) Thakur, I.; Örmeci, B.; Verma, A. Inactivation of E. coli in water employing Fe-TiO2 composite incorporating in-situ dual process of photocatalysis and photo-Fenton in fixed-mode. *J. Water Process Eng.* **2020**, *33*, No. 101085.
(68) Ness, S.; Martin, R.; Kindler, A. M.; Paetzel, M.; Gold, M.; Jensen, S. E.; Jones, J. B.; Strynadka, N. C. Structure-based design guides the improved efficacy of deacylation transition state analogue inhibitors of TEM-1 β-lactamase. *Biochemistry* **2000**, *39*, 5312−5321.
(69) Williamson, G. K.; Hall, W. H. X-ray line broadening from filed aluminium and wolfram. *Acta Metall.* **1953**, *1*, 22−31.
(70) Kubelka, P. New Contributions to the Optics of Intensely Light-Scattering Materials. Part I. *J. Opt. Soc. Am.* **1948**, *38*, 448−457.
(71) Shirley, D. A. High-resolution X-ray photoemission spectrum of the valence bands of gold. *Phys. Rev. B* **1972**, *5*, No. 4709.

https://doi.org/10.1021/acsomega.1c03102
ACS Omega 2021, 6, 26108−26118